Focus: Two-dimensional electron-electron double resonance and molecular motions: The challenge of higher frequencies

John M. Franck, Siddarth Chandrasekaran, Boris Dzikovski, Curt R. Dunnam, and Jack H. Freed[a)]

Department of Chemistry and Chemical Biology and National Biomedical Center for Advanced ESR Technology, Cornell University, Ithaca, New York 14853, USA

(Received 3 February 2015; accepted 31 March 2015; published online 21 April 2015)

The development, applications, and current challenges of the pulsed ESR technique of two-dimensional Electron-Electron Double Resonance (2D ELDOR) are described. This is a three-pulse technique akin to 2D Exchange Nuclear Magnetic Resonance, but involving electron spins, usually in the form of spin-probes or spin-labels. As a result, it required the extension to much higher frequencies, i.e., microwaves, and much faster time scales, with $\pi/2$ pulses in the 2-3 ns range. It has proven very useful for studying molecular dynamics in complex fluids, and spectral results can be explained by fitting theoretical models (also described) that provide a detailed analysis of the molecular dynamics and structure. We discuss concepts that also appear in other forms of 2D spectroscopy but emphasize the unique advantages and difficulties that are intrinsic to ESR. Advantages include the ability to tune the resonance frequency, in order to probe different motional ranges, while challenges include the high ratio of the detection dead time *vs.* the relaxation times. We review several important 2D ELDOR studies of molecular dynamics. (1) The results from a spin probe dissolved in a liquid crystal are followed throughout the isotropic → nematic → liquid-like smectic → solid-like smectic → crystalline phases as the temperature is reduced and are interpreted in terms of the slowly relaxing local structure model. Here, the labeled molecule is undergoing overall motion in the macroscopically aligned sample, as well as responding to local site fluctuations. (2) Several examples involving model phospholipid membranes are provided, including the dynamic structural characterization of the boundary lipid that coats a transmembrane peptide dimer. Additionally, subtle differences can be elicited for the phospholipid membrane phases: liquid disordered, liquid ordered, and gel, and the subtle effects upon the membrane, of antigen cross-linking of receptors on the surface of plasma membrane, vesicles can be observed. These 2D ELDOR experiments are performed as a function of mixing time, T_m, i.e., the time between the second and third $\pi/2$ pulses, which provides a third dimension. In fact, a fourth dimension may be added by varying the ESR frequency/magnetic field combination. Therefore, (3) it is shown how continuous-wave multifrequency ESR studies enable the decomposition of complex dynamics of, e.g., proteins by virtue of their respective time scales. These studies motivate our current efforts that are directed to extend 2D ELDOR to higher frequencies, 95 GHz in particular (from 9 and 17 GHz), in order to enable multi-frequency 2D ELDOR. This required the development of quasi-optical methods for performing the mm-wave experiments, which are summarized. We demonstrate state-of-the-art 95 GHz 2D ELDOR spectroscopy through its ability to resolve the two signals from a spin probe dissolved in both the lipid phase and the coexisting aqueous phase. As current 95 GHz experiments are restricted by limited spectral coverage of the $\pi/2$ pulse, as well as the very short T_2 relaxation times of the electron spins, we discuss how these limitations are being addressed. © *2015 AIP Publishing LLC.* [http://dx.doi.org/10.1063/1.4917322]

I. INTRODUCTION

Spin-label ESR spectroscopy has been widely used and demonstrated as a powerful tool to investigate the local dynamics and structure of complex fluids such as liquid crystals, model and biological membranes, polymers, proteins, and protein complexes.[1–7] An ESR spectrum provides a view of molecular motion. Modern simulation and fitting techniques can unlock a wealth of detailed information from these views. Two separate strategies for further extending the capabilities of ESR have emerged: multi-frequency ESR and two-dimensional electron-electron double resonance (2D ELDOR).

Multi-frequency ESR, achieved by acquiring a series of spectra at different resonance frequencies, sensitively detects and discriminates motions occurring on different time scales. Continuous-wave (cw) ESR has been successfully extended to high magnetic fields and frequencies,[1,8] leading to ESR line shapes with greatly improved orientational resolution that also provide a better insight into faster molecular dynamics.[1,6,9–11] Thus, one can design multi-frequency ESR experiments that unravel the details of dynamical modes of complex systems.[1,6,9,10,12]

a)Electronic mail: jhf3@cornell.edu

2D ELDOR studies on complex fluids and macromolecules disentangle the homogeneous broadening, which provides insight into molecular motions, from the inhomogeneous broadening, which relates to local structure and ordering.[1,13–18] Furthermore, it supplies cross-peaks that directly report on the relative diffusive motions of spin-bearing molecules (cf. background section) and rotational motions of labeled biomolecules that can be as slow as tens of microseconds (limited only by the T_1). Recent technological developments[19–21] have begun to lead to the capability of performing 2D ELDOR on complex fluids at high frequency (95 GHz), thus combining the virtues of 2D ELDOR with those of multi-frequency ESR.[6,10,19,20]

In this paper, we describe the challenges required to bring 2D ELDOR to the mm-wave regime and our current progress towards addressing them. We begin with an overview of the background of 2D ELDOR, including the underlying theory and earlier motivating experiments at standard ESR frequencies of 9 and 17 GHz. The theoretical prediction and interpretation require a special analysis developed by Freed and coworkers based on the stochastic Liouville equation (SLE).[22] Among other benefits, this method permits one to simulate spectra in the slow-motional regime, where other methods, such as Redfield theory, are no longer valid. We outline the fundamental concepts behind this approach, which has been effectively extended to predict 2D ELDOR spectra[23] and successfully applied to a variety of experiments performed at conventional ESR frequencies (9 and 17 GHz).[1,15–18] Then, we summarize the current state-of-the-art and the remaining technical challenges involved in successfully implementing multi-frequency 2D ELDOR experiments. We also note recent progress we have made in improving the computational algorithms to enable the simulation of high-frequency 2D-ESR spectra over the whole motional range.

ESR provides complementary information to that available from other spectroscopic techniques.[24] For instance, while particular variants of IR and fluorescence spectroscopy allow one to probe the fluctuations and reorganization of the solvent,[25–27] ESR is particularly good a probing changes in ordering,[17,28,29] e.g., of lipid bilayers, in response to changes in the solvent or composition and is sensitive to changes in structure and local dynamics that occur in association with conformational rearrangement,[1,5,30,31] allowing one to track motions over longer time scales than these other methods. Like many other modern forms of spectroscopy, multi-dimensional ESR makes frequent use of the stimulated echo and involves the concepts of rephasing and non-rephasing signals. However, as ESR typically involves only two spin transition levels [like Nuclear Magnetic Resonance (NMR)] with well understood and quantifiable interactions, this avoids, for example, the complexity that hot bands introduce into IR spectroscopy or that multiple transitions can introduce into UV-visible spectroscopy. ESR also features a unique probe moiety or molecule, thus avoiding the complexity, introduced by many similar spin centers, characteristic of NMR. The ESR transition frequencies do depend upon molecular orientations in a precise manner. Thus, one can focus on accurately and rigorously simulating the ESR spectrum to extract a wealth of detailed information about molecular dynamics and ordering.[32]

II. 2D FOURIER TRANSFORM (FT) ESR AND DYNAMICS IN COMPLEX FLUIDS: BACKGROUND AND THEORY

A. Background

2D NMR was first developed by Ernst and coworkers in 1976.[33] In 2D NMR, one uses nonselective radiofrequency (rf) pulses to successfully irradiate the entire spectrum and to collect the data shortly after pulse application. This process introduces coherences simultaneously to all spectral components and enables the observation of coherence transfer between these components. Ernst and Jeener subsequently showed how magnetization transfer could also be studied in this manner,[34] while a cw electron-electron double resonance experiment had previously been introduced by Hyde, Chien, and Freed.[35] Nonetheless, as compared to 2D NMR, it took another ten years for 2D-ESR to incorporate these ideas,[36] for the simple reason that the ESR experiment is more difficult to carry out. In the case of ESR, microwaves are used rather than the rf waves used in NMR. Also, the ESR relaxation times are orders of magnitudes faster, ESR pulse widths are orders of magnitude shorter, and the spectral bandwidths that must be covered are orders of magnitude wider. Consequently, it proved necessary to first develop FT techniques in ESR. Modern FT-ESR appeared in several laboratories, including ours, in the 1984-1988 period.[36–38] The 2D-FT-ESR experiments conducted at Cornell consisted of a 2D-ESR experiment, appropriately called spin-echo-correlated spectroscopy (SECSY) which utilizes two $\pi/2$ pulses, and a 2D-exchange experiment which utilizes three $\pi/2$ pulses, now referred to as 2D ELDOR.[36,39] In 2D ELDOR, very short pulses are used which simultaneously excite all the frequencies in the ESR spectrum in a coherent fashion. This leads to auto-peaks which provide the normal ESR spectral lines and cross-peaks between all pump and observing frequencies. The sequence of $\pi/2$-pulses and respective time delays for 2D ELDOR is shown in Fig. 1(a). The 2D spectrum is obtained by Fourier transforming with respect to the times t_1

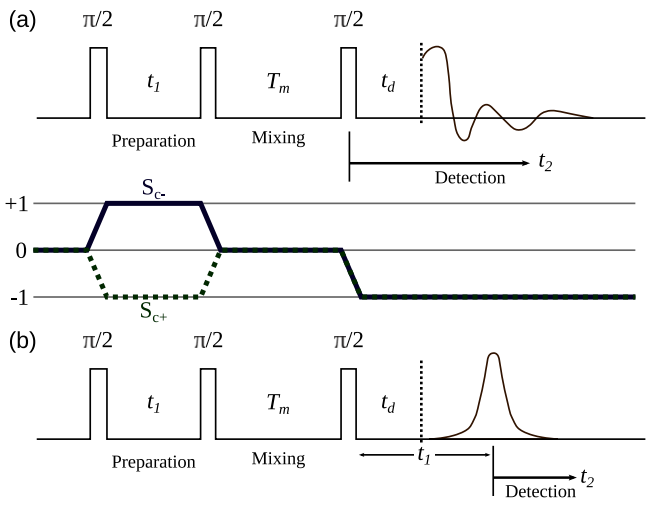

FIG. 1. The pulse sequences for (a) the standard 2D ELDOR experiment and (b) SECSY format of 2D ELDOR experiments. The two coherence pathways for this experiment are also shown.

and t_2. The "real-time" evolution of the 2D ELDOR spectrum is obtained by stepping out the mixing-time T_m. Another mode of performing this experiment is shown in Fig. 1(b), and we refer to it as 2D ELDOR in the SECSY mode.

With SECSY, it was possible to obtain homogeneous T_2 values from the whole spectrum simultaneously from an (inhomogeneously broadened) ESR signal. The first FT-based 2D ELDOR experiment goes beyond this and exhibits cross-peak development that results from Heisenberg spin-exchange. To make the technique of 2D ELDOR generally applicable, sophisticated phase-cycling was introduced on the technical side, whilst on the theoretical side, a full analysis was developed for the fast-motional 2D spectra, taking into account the generation of cross-peaks by the Heisenberg exchange (HE) and electron-nuclear dipolar (END) terms. Additional studies explored how to distinguish between the respective contributions to enable quantitative measurements of HE and of END terms in a liquid crystal.[40] The measurement of END terms led to sophisticated insights into molecular motions in ordered fluids that could not be obtained with cw-ESR. The measurement of rates of chemical exchange in a semi-quinone system was also demonstrated by using 2D ELDOR.[38]

Subsequently, 2D ELDOR was further developed to address the slow-motion regime (i.e., the regime where Redfield theory is no longer valid). This was accomplished by increasing the spectral coverage to 250 MHz, enhancing the data-acquisition rates, significantly reducing the spectrometer dead times,[41,42] and developing the general theory for the quantitative analysis of 2D spectra.[23] Complex fluids could then be studied in detail, including phospholipid membrane vesicles,[14,43] liquid crystals,[16,32] and liquid-crystalline polymers.[15] Simultaneous fits of 2D ELDOR data at several mixing times, T_m, provide a third dimension in that one monitors how the cross-peaks grow in relation to the auto-peaks with increasing mixing time, as shown in Fig. 2 for a liquid-crystalline phase of lipid vesicles compared to the liquid-ordered (LO) phase. This information provides quantitative information on the nuclear spin-flip-inducing processes of both HE, which is related (via intermolecular collisions) to translational diffusion, and the intramolecular END interaction, which is related to tumbling motions. We now turn to the underlying theory of 2D ELDOR.

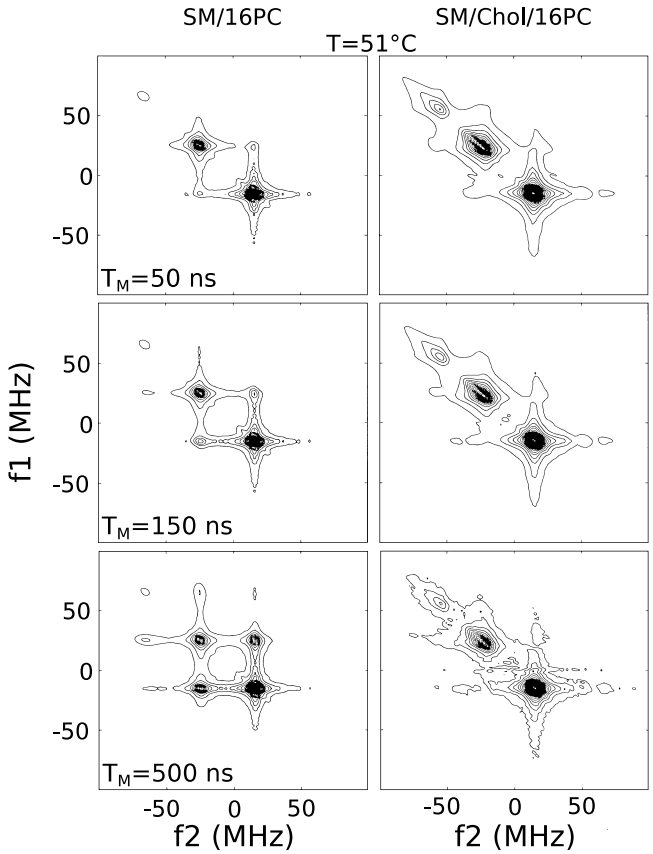

FIG. 2. 2D ELDOR signals at 17.3 GHz versus mixing time, T_m, of 16-PC in liquid-crystalline phase from pure lipid vesicles (left column) compared with 16 PC in liquid-ordered phase (right column) from 1:1 ratio lipid to cholesterol[17] at 51 °C. Modified with permission from J. H. Freed, Annu. Rev. Phys. Chem. **51**, 655 (2000). Copyright 2000 by Annual Reviews.

B. SLE to describe ESR spectra

The application of the stochastic Liouville equation to the calculation of ESR line shapes was introduced in 1971,[44] and since then has been extensively developed.[22,23,45–50] In additional to standard quantum-mechanical spin operators, the SLE includes a classical diffusion operator Γ_Ω that operates on the continuous space spanned by the Euler angles (Ω) that describe the relative orientations between the fluctuating molecular frame (MF) and the laboratory frame (LF). This allows one to define $\hat{\rho}(\Omega,t)$, which is a density operator describing the sub-ensemble of spin-bearing molecules with orientation Ω and which implicitly contains the probability distribution, $P(\Omega,t)$, for this orientation. A quantitative treatment of slow-motional ESR is then accomplished by solving the SLE,

$$\frac{\partial \hat{\rho}(\Omega,t)}{\partial t} = -i\left[\hat{H},\hat{\rho}(\Omega,t)\right] - \Gamma_\Omega \hat{\rho}(\Omega,t). \tag{1}$$

Note that (i) the standard spin density operator is obtained by averaging $\hat{\rho}(\Omega,t)$ over all Ω : $\hat{\rho}(t) = \int \hat{\rho}(\Omega,t)\,d\Omega = \langle \hat{\rho}(\Omega,t)\rangle_\Omega$ and (ii) tracing over the electron and nuclear spin states reduces the $\hat{\rho}(\Omega,t)$ to $\mathrm{Tr}[\hat{\rho}(\Omega,t)] = P(\Omega,t)$ (a scalar function).

The spin Hamiltonian in Eq. (1), which consists of hyperfine (hf) and Zeeman terms that exhibit orientational anisotropy, can be expressed as

$$\hat{H} = \sum_{l,m,m',\mu} \hat{A}^{(l,m)}_{\mu,LF} \mathscr{D}^{(l)}_{m,m'}(\Omega_{LM})\, F^{(l,m')^*}_{\mu,MF}, \tag{2}$$

where the $\hat{A}^{(l,m)}_{\mu,LF}$ are the irreducible components of the spin tensor with spin operators defined in the LF, in which the z-axis is along the external magnetic field, B_0; the subscript μ refers to the type of magnetic interaction (g-tensor or hf-tensor), whose irreducible tensor coefficients are given by $F^{(l,m')}_{\mu,MF}$ and are fixed in the MF; the $\mathscr{D}^{(l)}_{m,m'}(\Omega_{LM})$ are the Wigner rotation matrix elements (with $|m|, |m'| \le l$ integers) which affect transformations of the matrix elements between the LF and MF; and in most cases, the Hamiltonian is limited to rank $l = 2$ interactions for convenience.

C. Matrix representation of the SLE operator $\hat{\mathcal{L}}$

Using superoperator notation, the SLE (Eq. (1)) can be expressed as

$$\begin{aligned}\frac{\partial\hat{\rho}(\Omega,t)}{\partial t} &= -i\left[\hat{H},\hat{\rho}(\Omega,t)\right] - \Gamma_{\mathbf{\Omega}}\hat{\rho}(\Omega,t)\\ &= \left(i\hat{\mathcal{H}}^{\times} - \Gamma_{\mathbf{\Omega}}\right)\hat{\rho}(\Omega,t)\\ &= \hat{\mathcal{L}}\hat{\rho}(\Omega,t),\end{aligned} \tag{3}$$

where the second equality defines the superoperator for the spin Hamiltonian, $\hat{\mathcal{H}}^{\times}$, and the third equality defines the stochastic Liouville superoperator, $\hat{\mathcal{L}}$.

In order to represent Eq. (3) in Liouville space as

$$\frac{\partial}{\partial t}|\rho(\Omega,t)\rangle\!\rangle = \hat{\mathcal{L}}|\rho(\Omega,t)\rangle\!\rangle, \tag{4}$$

we seek a finite basis $|\sigma_i(\Omega)\rangle\!\rangle$ to represent $|\rho(\Omega,t)\rangle\!\rangle$ as a vector, $\vec{\rho}$, with elements $\rho_i = \langle\!\langle\sigma_i(\Omega)|\rho(\Omega,t)\rangle\!\rangle$ and $\hat{\mathcal{L}}$ as a matrix, $\mathbf{L}$, with elements $(L_{i,j} = \langle\!\langle\sigma_i|\hat{\mathcal{L}}|\sigma_j\rangle\!\rangle)$.

We first consider the basis for the Liouville spin states. Following standard notation, we map operators, $\hat{A}$, onto states, $\hat{A} \mapsto |A\rangle\!\rangle$, in Liouville space, where the inner product is defined by the adjoint and trace: $\langle\!\langle A|B\rangle\!\rangle = \mathrm{Tr}[\hat{A}^{\dagger}\hat{B}]$. We denote Liouville spin states corresponding to transition operators, $|m\rangle\langle m'|$, as follows:

$$\begin{aligned}|m\rangle\langle m'| &\mapsto |m,m'\rangle\!\rangle\\ &= |p,q\rangle\!\rangle,\end{aligned} \tag{5}$$

where m can be the quantum numbers of either the electron spin (typically, $S = 1/2$, $m_s = -1/2, 1/2$) or nuclear spin (for example, $I = 1$, $m_I = -1, 0, 1$) states and, for the case of a multiple-spin system, one can form direct products of the form of Eq. (5). On the second line of Eq. (5), we have defined $p^s = m_s - m'_s$, $p^I = m_I - m'_I$, $q^s = m_s + m'_s$, and $q^I = m_I + m'_I$. Note that p^s defines the coherence order for the electron spins: $p^s = 0$ corresponds to the diagonal type elements of the density matrix, whereas $p^s = \pm 1$ corresponds to off-diagonal matrix elements—for example, those between which microwave irradiation induces transitions.

To account for the orientational degrees of freedom, we provide an orthonormal basis set for the diffusion operator, $\Gamma_{\mathbf{\Omega}}$, to operate on:

$$\Phi^{(L)}_{M,K}(\Omega) = \mathcal{D}^{(L)}_{M,K}(\Omega)\sqrt{\frac{2L+1}{8\pi^2}}, \tag{6}$$

where the $\mathcal{D}^{(L)}_{M,K}$ are again the Wigner rotation coefficients, and the second factor after the equality is a normalization factor. While there are infinitely many choices for L, we can choose a finite basis by truncating to appropriate maximum values of L, M, and K. We can then define a convenient orthonormal basis set composed of the Liouville states,

$$|\sigma_i(\Omega)\rangle\!\rangle = |p^s,q^s;p^I,q^I\rangle\!\rangle\Phi^{(L)}_{M,K}(\Omega), \tag{7}$$

where the semicolon indicates a direct product between the electronic and nuclear spin states and the index i ranges over all possible combinations of p^s, q^s, p^I, q^I, L, M, and K. Note the simple relationship between the basis states and the Hamiltonian of Eq. (2),

$$|A^{(l,m)}_{\mu,LF}\rangle\!\rangle \propto \sum_{q^s,q^I}|p^s,q^s;q^I,p^I\rangle\!\rangle, \tag{8}$$

which simplifies calculation of the Hamiltonian superoperator. Schneider and Freed[22,46] describe the details of calculating slow-motional ESR line shapes for a nitroxide radical in solution.

D. Solving the SLE

1. Coherence sub-matrices

The basis set required to represent the stochastic Liouville (SL) superoperator is usually very large, which can require rather exorbitant times to diagonalize the SL matrix, $\mathbf{L}$. In the usual case of high magnetic fields and when no microwave pulse is present, the SL matrix is block-diagonal with respect to the coherence order of the electron spin, i.e., p^s. For $S = 1/2$, we distinguish between the submatrices $\mathbf{L}_{\pm 1}$ (spanned by the off-diagonal subspaces $p^s = \pm 1$) and $\mathbf{L}_0$ (spanned by the diagonal subspace $p^s = 0$). The three matrices can be diagonalized separately by different complex orthogonal transformations,

$$\mathbf{O}^{tr}_{p^s}\mathbf{L}_{p^s}\mathbf{O}_{p^s} = \mathbf{\Lambda}_{p^s}, \tag{9}$$

where $p^s = 0, \pm 1$, $\mathbf{O}_{p^s}$ is the complex orthogonal matrix formed from the eigenvectors, and $\mathbf{\Lambda}_{p^s}$ is the eigenvalue matrix for coherence order p^s. (Note that SL operator of Eq. (3) is not Hermitian, but complex symmetric, or may be rendered so by an appropriate similarity transformation: $\mathbf{S} = \mathbf{HU}$, where $\mathbf{H}$ is Hermitian and $\mathbf{U}$ is unitary[22]—see also Eq. (13) and below Eq. (16).)

2. Lanczos algorithm (LA)

The diagonalization of each $\mathbf{L}_{p^s}$ submatrix is performed by using the Lanczos algorithm.[22,23,46,48] Given that the SL matrix is sparse, one can achieve order-of-magnitude (and even greater) reduction in computation time by employing the LA. One exploits the starting vector, $\vec{\nu}$ $(\nu_i = \langle\!\langle\sigma_i|\nu\rangle\!\rangle)$, to select out the small sub-set of vectors, known as Lanczos vectors, which span the sub-space required to calculate the ESR spectrum. The current method uses an objective criterion to determine when a sufficient sub-space, of much smaller dimensionality, has been generated. This subspace is simultaneously projected out, and the reduced SL matrix is converted to tri-diagonal form, which is then easily diagonalized.[22] In this manner, a greatly reduced number of multiplications are required. In modified form, the LA can also be used to provide an objective method to prune the original set of basis vectors down to the minimum set needed to represent the relevant eigenvectors.

To simulate pulsed 2D experiments, we require the pulse propagator, $\hat{\mathcal{P}}$. For a particular coherence pathway, we may write $\hat{\mathcal{P}}_{(p^s_1 \leftarrow p^s_2)}$ as the corresponding pulse propagator, where p^s_1 and p^s_2 are the coherence orders after and before the pulse, respectively. In the case of a 90° pulse, the matrix representation of each such pulse propagator is proportional to the unit matrix in the sub-block that connects the associated sub-space(s) of the SLE and is zero elsewhere (see Ref. 23).

The 2D-ESR signal is given by

$$S_{c\pm1}^{\mathrm{ELDOR}} \propto \langle\langle \nu_{-1}|\hat{O}_{-1}\exp(-\hat{\Lambda}_{-1}t_2)\hat{O}_{-1}^{tr}\hat{\mathcal{P}}_{(-1\leftarrow 0)} \times \hat{O}_0\exp(-\hat{\Lambda}_0 T_m)\hat{O}_0^{tr}\hat{\mathcal{P}}_{(0\leftarrow\mp1)} \times \hat{O}_{\mp}\exp(-\hat{\Lambda}_{\mp}t_1)\hat{O}_{\mp}^{tr}|\nu_{\mp1}\rangle\rangle, \quad (10)$$

where $|\nu_{\mp1}\rangle\rangle = \hat{\mathcal{P}}_{(\mp1\leftarrow 0)}|\hat{\rho}_0\rangle\rangle$ is the density operator after the first $\pi/2$ pulse, and t_1, t_2, and T_m are illustrated in Fig. 1. It can be calculated once (i) the matrix representations, $\mathbf{L}_0$, $\mathbf{L}_{\pm1}$, in the diagonal ($p^s = 0$) and off-diagonal ($p^s = \pm1$) subspaces of the operator are obtained; (ii) the matrix representations of the pulse propagators that switch between the sets of subspaces are obtained (from Eq. (11) of Ref. 23); and (iii) the eigenvalues and eigenvectors of the SL matrix are found.

There are two coherence pathways shown in Fig. 1 and given by Eq. (10): S_{c+} and S_{c-}. The former does not result in any echo-type refocusing and we refer to it as free induction decay (FID)-like. The latter does have refocusing and yields a "stimulated echo." Thus, S_{c-} is the "rephasing" signal, while S_{c+} is the "non-rephasing" signal.

E. Diffusion in anisotropic media

1. The SLE

In anisotropic media, such as liquid crystals or membranes, or in the presence of side-chain motion in proteins, the orientational distribution of the spin probe is not isotropic. In that case, its equilibrium distribution, $P_{eq}(\Omega)$, can be derived from an orientational potential energy, $U(\Omega)$, which is the potential of mean torque experienced by it,

$$P_{eq}(\Omega) = \frac{\exp\left(\frac{-U(\Omega)}{k_BT}\right)}{\int \exp\left(\frac{-U(\Omega)}{k_BT}\right) d\Omega}, \quad (11)$$

where k_B is Boltzmann's constant and T is the temperature.

The diffusion operator becomes

$$\Gamma_{\mathbf{\Omega}} = \nabla_{\mathbf{\Omega}} \cdot \mathbf{R} \cdot \left[\nabla_{\mathbf{\Omega}} + \frac{1}{k_BT}\nabla_{\mathbf{\Omega}} \cdot U(\Omega)\right]. \quad (12)$$

Here, $\mathbf{R}$ is the rotational diffusion tensor. Equation (12) is known as a Smoluchowski equation. It has the property that any initial $P(\Omega,0)$ that evolves according to $\partial P/\partial t = -\Gamma_{\mathbf{\Omega}}P(\Omega,t)$ will converge to $\lim_{t\to\infty} P(\Omega,t) = P_{eq}(\Omega)$. In other words, $P_{eq}(\Omega)$ is an eigenfunction of $\Gamma_{\mathbf{\Omega}}$ with zero eigenvalue. $\Gamma_{\mathbf{\Omega}}$, as given by Eq. (12), is non-symmetric but can be converted into the symmetric form by the following Hermitian transformation:[45]

$$\tilde{\Gamma}_{\mathbf{\Omega}} = P_{eq}(\Omega)^{-1/2}\Gamma_{\mathbf{\Omega}}(\Omega)P_{eq}(\Omega)^{1/2}, \quad (13)$$

which yields

$$\tilde{\Gamma}_{\mathbf{\Omega}} = \left[\nabla_{\mathbf{\Omega}} - \frac{\nabla_{\mathbf{\Omega}}}{k_BT}\right] \cdot \mathbf{R} \cdot \left[\nabla_{\mathbf{\Omega}} + \frac{\nabla_{\mathbf{\Omega}}}{k_BT}\right]. \quad (14)$$

The diffusion equation (Eq. (14)) may be solved for $\tilde{P}(\Omega,t) = P_{eq}^{-1/2}(\Omega)P(\Omega,t)$. The symmetric matrix $\tilde{\Gamma}_{\mathbf{\Omega}}$ can be diagonalized after calculating its matrix elements explicitly in the basis formed by the functions $\Phi_{M,K}^{L}(\Omega)$ given by Eq. (6). The new SLE operator becomes

$$\tilde{\hat{\mathcal{L}}} = i\hat{\mathcal{H}} - \tilde{\Gamma}_{\mathbf{\Omega}} \quad (15)$$

for which the new starting vector is

$$|\tilde{\nu}\rangle\rangle = P_{eq}^{-1/2}(\Omega)|\nu\rangle\rangle. \quad (16)$$

Finally, the expression for the 2D ELDOR (Eq. (10)) may be solved after the replacement: $|\nu\rangle\rangle \to |\tilde{\nu}\rangle\rangle$ and $\Gamma_{\mathbf{\Omega}} \to \tilde{\Gamma}_{\mathbf{\Omega}}$. (Another requirement to render the SL matrix to be complex symmetric is for the basis sets to be made to obey time reversal symmetry by the appropriate unitary transformation.[22])

2. The potential function, $U(\Omega)$, and the ordering tensor S

The potential energy operator, $U(\Omega)$, can be expanded in terms of the Wigner rotation matrix elements $\mathcal{D}_{M,K}^{(L)}(\Omega)$ as follows:

$$-\frac{U(\Omega)}{k_BT} = \sum_{L,M,K} c_{M,K}^{L}\mathcal{D}_{M,K}^{(L)}(\Omega). \quad (17)$$

The resulting ordering $\mathbf{S}$ tensor elements can be obtained by using $P_{eq}(\Omega)$ as follows:

$$S_0 = \left\langle \mathcal{D}_{0,0}^{(2)} \right\rangle = \int P_{eq}(\Omega)\mathcal{D}_{0,0}^{(2)}(\Omega)\, d\Omega \quad (18)$$

$$S_2 = \left\langle \mathcal{D}_{0,2}^{(2)} + \mathcal{D}_{0,-2}^{(2)} \right\rangle. \quad (19)$$

Since $\mathbf{S}$ is a traceless 2nd rank tensor, only S_0 and S_2 are needed in its principal axis frame.

In actual applications, the expansion of $\hat{H}$ in Eq. (2) and the use of $\Omega \to \Omega_{LG}$ are usually too simple a diffusive model to explain experiments. We now introduce the Microscopic Order and Macroscopic Disorder (MOMD) model and the Slowly Relaxing Local Structure (SRLS) model.

3. Reference frames used in the MOMD and SRLS models

Various reference frames, which are illustrated in Fig. 3, are required to fully model the various motions and interactions involved in the SLE and are defined here: the **LF** is defined with respect to the external magnetic field, $\hat{B}_0$, whose direction is used as its z-axis. The local director, $\hat{n}$, defines the **director frame (DF)**, which, in general, is tilted relative to the magnetic field by the angle ψ and is obtained by transformation by the set of Euler angles $\Psi_{L\to D}$ from LF to DF. In membranes, $\hat{n}$ is usually taken as parallel to the local membrane normal; in a protein, it represents the preferred orientation of the spin label side-chain, which is a local direction in the protein that is fixed relative to the protein backbone;[12,49] and in a complex fluid, it would be determined by the instantaneous orientation of the solvent "cage."[16,48] In MOMD, the $\Psi_{L\to D}$ Euler angles are "frozen," i.e., time independent and usually randomly oriented. In SRLS, they are time-dependent due to the slower motion of the larger body. The principal axes of the molecular diffusion tensor (usually taken as the principal axes of the ordering tensor of the molecule or spin-bearing moiety—see Eqs. (18) and (19)) define the **MF**, which is fixed within the molecule.

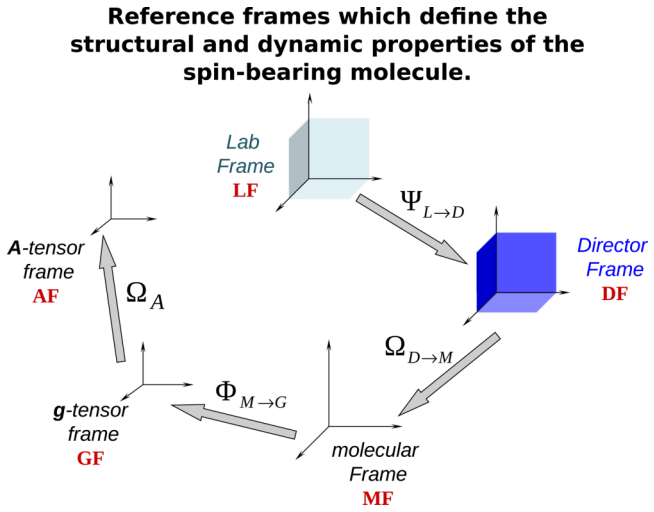

FIG. 3. Reference frames that define the orientation of a sample to study its structural and dynamic properties. (i) Lab frame (LF) is defined with respect to the external magnetic field, whose direction is used as its z-axis; (ii) director frame (DF) is defined by the local director, $\hat{n}$, tilted relative to the magnetic field by the angle ψ and obtained by the transformation by the set of Euler angles $\Psi_{L\to D}$ from LF to DF; (iii) molecular frame (MF) is fixed within the molecule and obtained by the transformation by the set of Euler angles $\Omega_{D\to M}$; (iv) g-tensor frame (GF), the principal-axes frame of the g-tensor of the unpaired electron is obtained using the transformation $\Phi_{M\to G}$ from MF to GF; (v) A-tensor frame (AF), defined by the principal-axes of the A-tensor, is obtained using Ω_A from GF to AF.

It is obtained by the transformation of $\Omega_{D\to M}$ from DF to MF. The *g*-**tensor frame (GF)** is the principal-axes frame of the *g*-tensor and is obtained by the transformation by the set of Euler angles $\Phi_{M\to G}$ from MF to GF. The **A-tensor frame (AF)** is defined by the principal-axes of the *A*-tensor (hf interaction) and is obtained by the transformation by the set of Euler angles Ω_A from GF to AF; however, the principal-axes of the *A*-tensor are typically found to be almost parallel to those of the *g*-tensor for nitroxide labels.

In order to define the orientation of the spin-bearing molecule, the typical molecular magnetic tensor in irreducible tensor notation is transformed from the GF to LF frame as follows:

$$F^{(2,m)^*}_{\mu,LF} = \sum_{m',m'',m'''} \mathcal{D}^{(2)}_{m,m'}(\Psi_{L\to D})\mathcal{D}^{(2)}_{m',m''}(\Omega_{D\to M}) \times \mathcal{D}^{(2)}_{m'',m'''}(\Phi_{M\to G})F^{(2,m''')^*}_{\mu,GF}, \quad (20)$$

which generalizes Eq. (2).

4. MOMD

It is often the case that the spin-labeled molecule will exhibit restriction of its motion because of the structure in its local surroundings (i.e., microscopic order), e.g., a labeled lipid molecule will orient relative to the lipid membrane normal at its site, which would itself be orientationally randomly distributed in a membrane vesicle. In another example, a spin label on a protein side-chain will be restricted in its motion to a limited range of orientations relative to the backbone. In the limit of very slow reorientation of the larger body (e.g., protein or lipid vesicle), one can employ MOMD to model the distribution of orientations of the spin labels in the ensemble relative to the main magnetic field (i.e., macroscopic disorder).[29,49] Specifically, one takes an average of the spectra from all orientations, ψ, which define the transformation angles $\Psi_{L\to D}$ that appear in Eq. (20), to obtain the composite MOMD spectrum, as follows:

$$I(\omega) = \int I(\omega,\psi)\sin(\psi)d\psi. \quad (21)$$

By definition, this spectrum is inhomogeneously broadened, but it happens in a characteristic manner, which depends on the ordering potential Eq. (17), or equivalently upon the ordering tensor **S**, for example, that given by Eqs. (18) and (19).

5. SRLS model

With the enhanced resolution offered by 2D ELDOR and also high-field high-frequency (HF-HF) ESR, more sophisticated models of molecular reorientation have been proposed to fit these ESR spectra. For example, the many-body problem of dealing with the microscopic details of fluids is approximated by a set of collective degrees of freedom that represent the main effects of the solvent on a rotating solute. These collective variables are modeled as a loose solvent "cage," which is considered to be relaxing slowly and within which the solute is assumed to be reorienting more rapidly. This so-called SRLS is obtained by generalizing the MOMD model by letting the Euler angles $\Psi_{L\to D}$ fluctuate in time due to the slow overall process; this may also be a slow tumbling of a vesicle or overall rotation of a protein.[48,51]

III. MOLECULAR DYNAMICS IN LIQUID CRYSTALS AND MEMBRANES: 2D ELDOR AT 17 GHZ

A. 2D ELDOR of complex fluids

2D ELDOR spectra are very sensitive to the properties of membrane vesicles, showing dramatic changes with modest variations in the membranes' properties. Moreover, such changes can even be detected visually from the spectral patterns by a simple inspection; an example is seen in Fig. 2, which shows the 2D ELDOR contour plots as a function of the mixing time, T_m, for the spin-labeled lipid, 1-palmitoyl-2-(16-doxyl stearoyl) phosphatidylcholine (16-PC) in pure lipid vesicles, in a standard liquid-crystalline phase, and also for a 1:1 lipid-cholesterol mixture, which exhibits a "LO" phase. The qualitative difference in the spectra indicates that the LO phase exhibits significantly greater ordering than the liquid crystalline phase, due to its increased microscopic ordering—hence macroscopic broadening of the spectrum. In addition, the LO phase exhibits a much slower development of cross-peaks as a function of T_m, due to a restricted range of orientational motion as a result of microscopic ordering.[17]

Complete averaging leads to homogeneous broadening, while a distribution of orientations in the ensemble, i.e., MOMD, causes complex inhomogeneous line shapes.[29,49] A second often-encountered source of inhomogeneous broadening is reorientation in the slow-motional regime, yielding incomplete averaging. Such slow-motional spectra are very sensitive to details of the molecular motions.

In complex fluids, it was found that the SRLS model was needed to simulate these slow-motional effects and analyze the 2D ELDOR spectra. A macroscopically aligned liquid crystal solvent, called 4O,8, exhibits many phases as a function of temperature, including isotropic (I), nematic (N), liquid-like smectic (S_A), solid-like smectic (S_B), and crystalline (C) phases. The SRLS model, in addition to including the macroscopic liquid-crystalline orienting potential, provides consistently better fits than can be obtained with the simpler MOMD model.[16,32] By studying a macroscopically aligned sample, one can obtain extensive relaxation, dynamic, and structural information which includes virtually all of the parameters obtainable from any ESR experiments on spin relaxation in a complex fluid! These ten parameters are as follows: the two-term (asymmetric) macroscopic ordering potential in the liquid crystalline phases, the axially symmetric diffusion tensor for the probe, its two-term orienting potential in the local structure or cage, the relaxation rate for the cage, the residual homogeneous T_2 due to processes other than the reorientational modulation of the ^{14}N dipolar and g-tensors, the residual (Gaussian) inhomogeneous broadening not due to the specific slow-motional contributions from the ^{14}N hf- and g-tensors, and the overall T_1 for the electron spins.

In Fig. 4, one sees some of the results from the study of a spin-labeled cholesterol analogue, cholestane, dissolved in 4O,8. Cholestane is highly ordered in 4O,8 and reports on the differences between the phases at a molecular level. In Fig. 4(a), one sees how neither of the rotational diffusion coefficients $R^0_{\|}$ and $R^0_{\perp}$ (the parallel and perpendicular components of $\mathbf{R}^0$) changes much as a function of temperature throughout the phases, though they do increase slightly during the N → S_A transition, presumably due to decreased friction in the more ordered S_A phase. Most interesting is the behavior of the motional rate of the cage, R^c. In the I, N, and S_A phases, R^c is at least an order of magnitude slower than that of the cholesterol probe, but upon entering the S_B phase, R^c decreases an order-of-magnitude further. To appreciate the origin of this decrease, one can examine the various potential terms. Fig. 4(b) shows the effects of the macroscopic alignment on the probe via the potential coefficients (which are given as multiples of k_BT) a^2_0 and a^2_2, while Fig. 4(c) shows the local fluctuating potential, or cage, via c^2_0 and c^2_2. Note that at the S_A → S_B transition, which is a liquid-like to solid-like smectic transition, the cage potential drops sharply and the macroscopic potential a^2_0 increases substantially. This is interpreted to mean that the spin label is no longer affected by local 4O,8 chain fluctuations, which freeze out, leading to macroscopic alignment.

The nature of the boundary lipid that coats a membrane protein is another interesting issue which could be studied by 2D ELDOR, as it was in a study of the peptide gramicidin A (GA) residing in a model membrane.[52] This study required 2D ELDOR at a higher resonance frequency of 17.3 GHz, in order to achieve increased signal-to-noise ratio (SNR), as well as reduced dead times (~25 – 30 ns),[53] so that one could discern the presence of two components, representing two populations of spin-labeled lipids. These are (i) the bulk component, which exhibited relatively fast dynamics, and (ii) the boundary lipid, which grows in as the GA is added, and

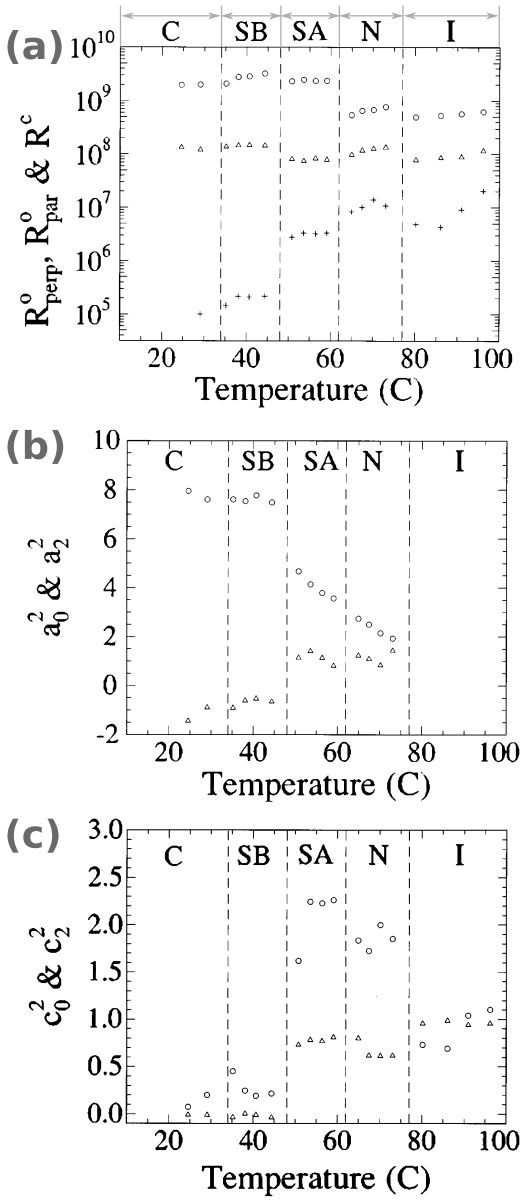

FIG. 4. (a) Rotational diffusion coefficients for the probe: $R^0_{\|}$ (open circles) and $R^0_{\perp}$ (open triangles), as well as the cage (plus signs), plotted as a function of temperature. (b) Mean field (macroscopic) orienting potential parameters: a^2_0 (open circles) and a^2_2 (open triangles) as a function of temperature. (c) Cage potential parameters: c^2_0 (open circles) and c^2_2 (open triangles) as a function of temperature (fits to SRLS model; adapted with permission from V. S. S. Sastry *et al.*, J. Chem. Phys. **105**, 5753 (1996); copyright 1996 by AIP Publishing LLC).

whose 2D ELDOR spectrum is undoubtedly that of a more slowly reorienting lipid, as expected. These spectra could be simulated with a physically meaningful model where the end-chains of the lipids are bent as they coat the GA. Such details of the dynamic structure of complex membrane systems can only be obtained using 2D ELDOR.

B. Improved resolution with the full S_{c-} method

In the 2D ELDOR studies shown in Figs. 2 and 4, the magnitude spectra were used, despite the fact that full complex S_{c-} data were acquired. This is because imperfect

spectral coverage from pulses of finite widths as well as finite spectrometer dead times leads to phase shifts along both frequency dimensions, which distort these spectra; however, the magnitude spectra are unaffected by this. Unfortunately, as is well known, magnitude spectra significantly reduce the spectral resolution relative to pure absorption spectra, so a new method was needed to recover this resolution.

A standard cw or a FID signal is composed of real and imaginary parts, wherein, by convention, we refer to the absorption as the real part and the dispersion as the imaginary part. For a 2D spectrum, it is typically possible to acquire the 2D real and imaginary components for both the echo-like (rephasing) S_{c-} and the FID-like (non-rephasing) S_{c+} components, previously expressed in Eq. (10) and illustrated in Fig. 1. Such a four-component dataset (real and imaginary for S_{c-} and S_{c+}) is referred to as a "hypercomplex" dataset, and it could be used to reconstruct a 2D spectrum with pure absorption line shapes. However, 2D ELDOR suffers from the difficulty that the full hypercomplex signal is not usually available, but only the S_{c-} component. This is the result of the presence of significant inhomogeneous broadening, which causes the S_{c+} component to decay much more rapidly than the S_{c-} component, often greatly reducing its amplitude by the end of the finite spectrometer dead time. A second problem is that the effect of the first-order phase shifts that arise from the finite spectrometer dead time and incomplete spectral coverage by pulses of finite width often cannot be directly used to correct the experimental spectra. That is, the complex 2D spectra are made up of many "dynamic spin packets," which are the eigenmodes of the SLE,[22] and each of which is a mix of absorptive and dispersive components. It is impossible to separate the various dynamic spin packets that make up the composite spectrum, and one must rely on the theoretical analysis.

To overcome both these difficulties, the "full S_{c-}" method, which utilizes both the real and imaginary components of the experimental S_{c-} signal, was developed.[54,55] The standard NLLS fitting package[46] was modified to include the phase corrections as additional fitting parameters in the nonlinear least-squares fitting of theory to experiment. The fitting procedure can thus take advantage of the greater resolution and detail supplied by the full complex data to yield the dynamic and ordering parameters. One can then use the resulting phase corrections from the fit to produce approximate pure absorption spectra from the original experimental data or one can generate the theoretical prediction of the pure absorption-mode spectrum from the fits to the model parameters.[18,54]

C. Two applications of the full S_{c-} method

In the first application, we have been able to obtain the phase diagram of 1,2-dipalmitoyl-sn-glycero-phosphatidyl-choline (DPPC)-cholesterol binary mixtures *vs.* temperature.[18] This phase diagram has regions corresponding to liquid-disordered, liquid-ordered, and gel phases. The 2D ELDOR spectra from the 16-PC spin label are very distinctive for these phases, especially in the absorption format. In Fig. 5, we show the "normalized" contour plots, which are obtained by taking Fourier-transformed data in the SECSY mode (see

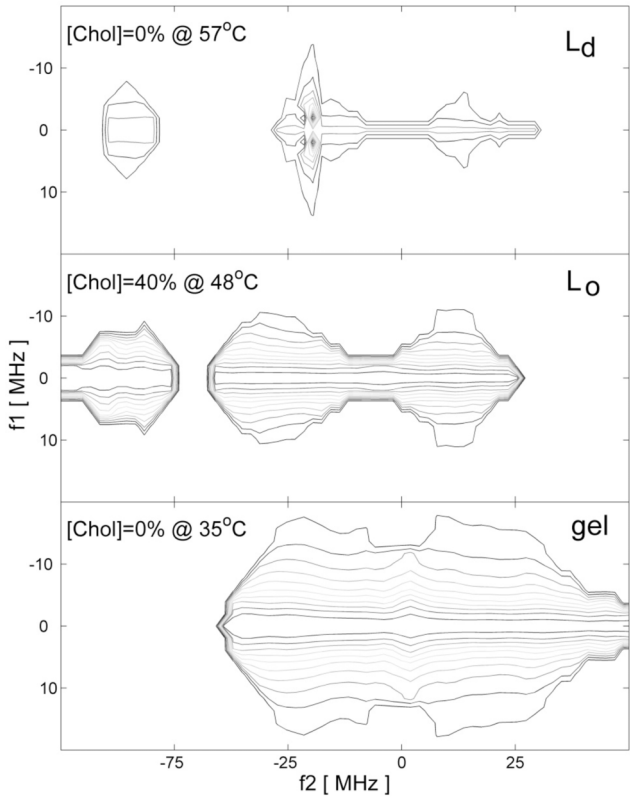

FIG. 5. Contour plots of the 3 lipid phases: approximate absorption 2D ELDOR spectra in the SECSY format (cf. Fig. 1), acquired from samples of 16-PC in DPPC-cholesterol vesicles, in the normalized contour presentation, which displays the homogeneous linewidths in the f_1 direction. The upper, middle, and lower contours represent L_d, L_o, and gel phases, respectively. Reprinted with permission from Fig. 5 of Y. W. Chiang *et al.*, Appl. Magn. Reson. **31**, 375 (2007). Copyright 2007 by Springer International Publishing AG.[56]

Fig. 1), then dividing by the $f_1 = 0$ spectrum, so that the resultant $f_1 = 0$ contour is simply a line of unity value, whose linewidth provides a comparison of the homogeneous linewidth (along f_1) at different locations of the ESR spectrum (along f_2). The L_d phase yields the signal with the narrowest homogeneous linewidths, whereas those from the gel phase are the broadest. In addition, the signal from all phases shows distinctive linewidth variations across the spectrum. A careful analysis of the 2D ELDOR spectra versus mixing time T_m and temperature has allowed us to characterize the respective single-phase regions, as well as the two-phase regions, leading to the phase diagram shown in Fig. 6, along with representative 2D ELDOR spectra. This phase diagram is in reasonably good agreement with previous studies, which however required several different physical techniques, as opposed to our application of just 2D ELDOR.[18] Here, the full S_{c-} method was crucial for reliably extracting the dynamic parameters and determining the dynamic structure over the whole phase diagram, especially in the two-phase coexistence regions.

In the second example, we have applied the full S_{c-} method to analyze the 2D ELDOR spectra we obtained from plasma membrane vesicles (PMV) from RBL-2H3 mast cells in order to investigate the dynamic structural changes upon antigen cross-linking of IgE receptors on the surface

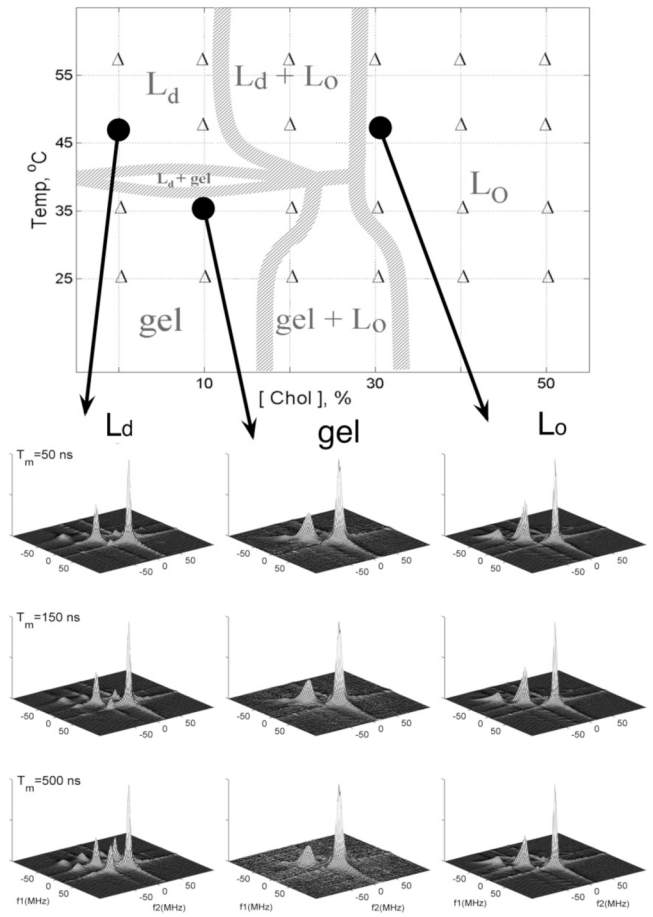

FIG. 6. (Top) Phase diagram of binary mixtures of DPPC-cholesterol containing 16-PC determined according to 2D ELDOR analysis. Triangles and filled circles indicate the compositions studied. (Bottom) 2D ELDOR spectra, from compositions as marked, show distinctive patterns and line shape variations for one to characterize the membrane phases. (Standard magnitude mode shown for convenience; reprinted with permission from Fig. 6 of Y. W. Chiang *et al.*, Appl. Magn. Reson. **31**, 375 (2007). Copyright 2007 by Springer International Publishing AG.[56])

of the PMV.[57] The 2D ELDOR spectra after cross-linking show small but significant changes, whereas the cw ESR does not. We found it difficult to obtain unambiguous fits to the spectra in the magnitude mode. However, with the full S_{c-} method, we were able to obtain good quality fits and to distinguish the small but significant changes in the PMV before and after cross-linking. The molecular dynamic and ordering parameters extracted from spectral fitting also enable us to characterize the heterogeneities in the PMV. We found it necessary to fit the spectra with two spectral components in order to achieve good fits to the full S_{c-} data. The ordering, given by the ordering parameter S_0, is found to be the best distinguishing feature between the coexisting components and to identify these components as corresponding to the L_d and L_o phases, whereas the rotational diffusion rates for both components are comparable. These two coexisting spectral components are shown in Fig. 7 in the absorption mode, as obtained from the best theoretical fits.

The populations of the coexisting components are found to change upon cross-linking. As shown in Fig. 8, the population of the L_o phase in both uncross-linked and cross-linked

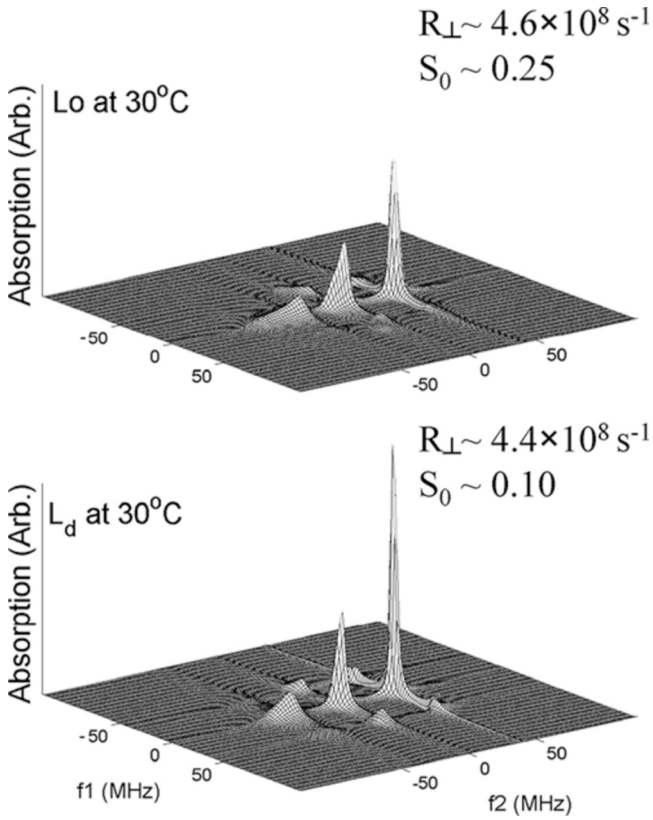

FIG. 7. The two 2D ELDOR pure absorption spectral components (in the SECSY mode) representing the coexisting L_o and L_d regions in the PMV. They were obtained from the best theoretical fit to the experimental spectrum for the un-cross-linked PMV at 30 °C for $T_m = 50$ ns. Reprinted with permission from Y.-W. Chiang *et al.*, J. Phys. Chem. B **115**, 10462 (2011). Copyright 2011 by American Chemical Society.

samples is found to increase modestly with increasing temperature. Upon cross-linking, the PMV tends to remodel itself to become more disordered, i.e., the population of the L_d component increases. Our results from 2D ELDOR provide significant further details about the membrane structural changes before and after cross-linking.

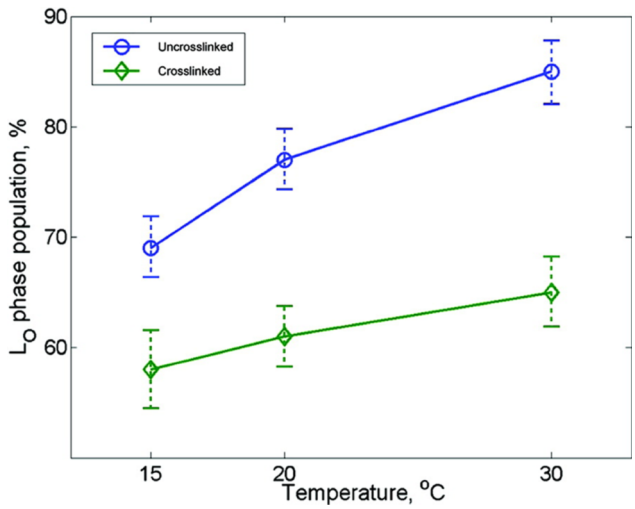

FIG. 8. The population of the L_o component, coexisting with the L_d, in the uncross-linked versus cross-linked PMV samples with respect to temperature. Reprinted with permission from Y.-W. Chiang *et al.*, J. Phys. Chem. B **115**, 10462 (2011). Copyright 2011 by American Chemical Society.

IV. MULTIFREQUENCY ESR TO UNRAVEL MOLECULAR MOTION

Figure 9 shows the experimental cw ESR spectra of perdeuterated tempone (PDT) spin probe dissolved in toluene at 250 GHz in various motional regimes: motional narrowing, slow motion, and the rigid limit as the temperature is reduced. Figure 10 shows a series of simulated multifrequency spectra covering the range of 15–2000 GHz for a spin-bearing molecule with a rotational correlation time of 1.7 ns, and it illustrates how a motional process that appears fast at lower frequencies will seem slow or rigid at higher frequencies. Thus, for complex systems, such as proteins or membranes, the slow overall and collective motions will be displayed better at lower frequencies, whereas the fast—typically more localized—motions will be more sensitively demonstrated at higher frequencies. Accordingly, the ESR frequency becomes another useful "dimension" for ESR, enabling one to separate out the modes of motion based on their respective time scales.

An example of multifrequency ESR for a spin-labeled protein at different temperatures is exhibited by the spectra in Fig. 11 of T4 lysozyme labeled at mutant site 131, acquired at four frequencies, ranging from 95 GHz to 240 GHz, and several temperatures. At 240 GHz, the overall rotation was too slow to significantly affect the spectrum, so that it is perceived to be in the rigid limit, and a good resolution of the faster internal dynamics is achieved. In the low frequency limit, the 9 GHz line shape data required the SRLS model to successfully obtain the rates for the global dynamics. The full multifrequency study yielded simultaneous quantitative fits using the SRLS model. In fact, it showed the existence of several types of internal motions for the spin-labeled T4 lysozyme.[12]

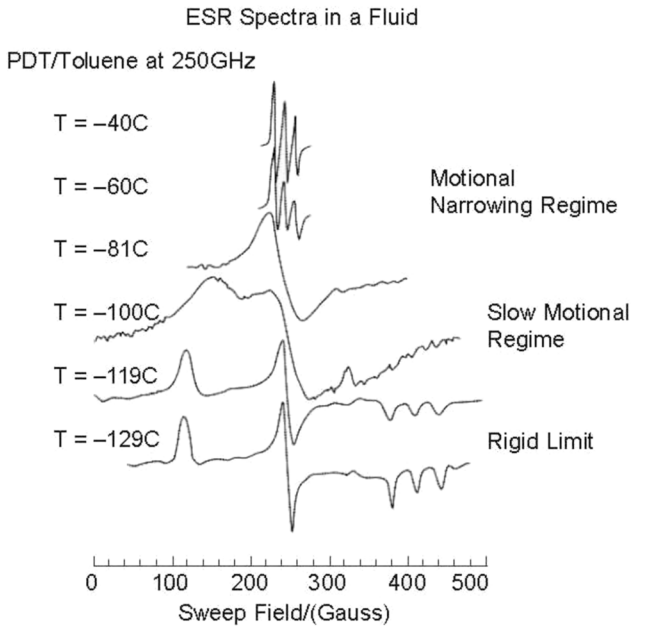

FIG. 9. ESR spectra of PDT/toluene at 250 GHz in various motional regimes: motional narrowing (−40 °C, −60 °C), slow motion (−81 °C, −100 °C), and rigid limit (−119 °C, −129 °C). Reproduced with permission from Fig. 11.1 of S. K. Misra and J. H. Freed, "Molecular motions," in *Multifrequency Electron Paramagnetic Resonance* (Wiley-VCH Verlag GmbH & Co. KGaA, 2011), pp. 497–544 (cf. Ref. 58). Copyright 2011 by Wiley-VCH Verlag GmbH & Co. KGaA.

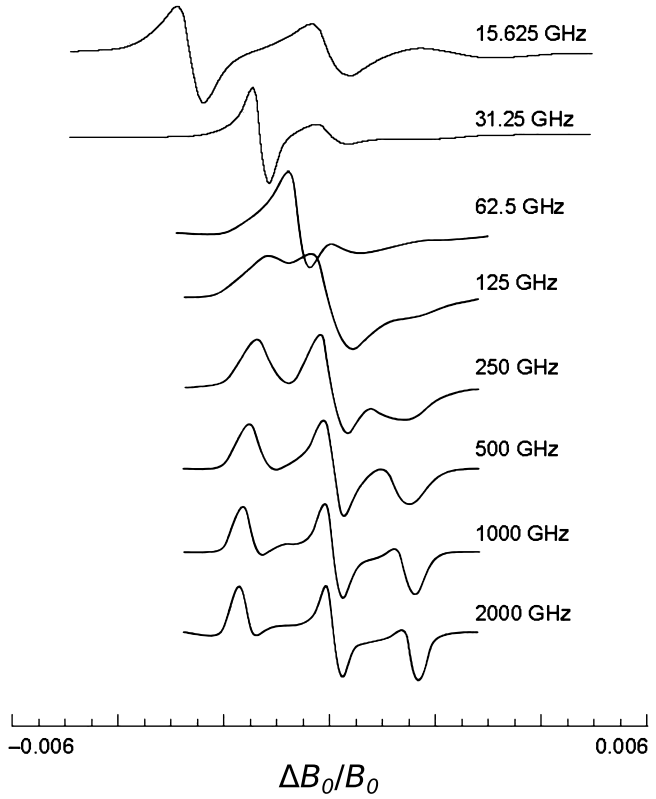

FIG. 10. Simulated first-derivative multifrequency ESR spectra for a nitroxide, reorienting with a rotational diffusion constant $R = 10^8\ s^{-1}$ (corresponding to rotational correlation time $\tau_R = 1.67$ ns) in the range 15–2000 GHz. From this, it is clear that a motional process that appears fast at lower frequencies will appear slow at higher frequencies.[13] Modified with permission from J. H. Freed, Annu. Rev. Phys. Chem. **51**, 655 (2000). Copyright 2000 by Annual Reviews.

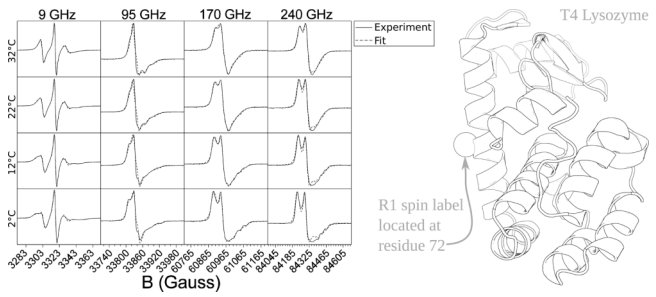

FIG. 11. An example of how multifrequency ESR distinguishes motion at different temperatures, as exhibited by the ESR spectra of T4 lysozyme spin-labeled at mutant site 72 at 9, 95, 170, and 240 GHz at 2, 12, 22, and 32 °C. (Left panel of figure adapted with permission from Z. Zhang *et al.*, J. Phys. Chem. B **114**, 5503 (2010). Copyright 2010 by American Chemical Society. Right panel of figure generated from PDB 1YLD, structure rendered by PyMOL, Schrödinger, LLC.)

V. TOWARDS MULTIFREQUENCY ELDOR: 95 GHZ 2D ELDOR

As we have seen, even in cw-mode, multi-frequency ESR enables one to separate the different components of

complex dynamics. We have also seen how the second spectral dimension, coupled with the capability of distinguishing homogeneous broadening, in 2D ELDOR greatly increases sensitivity to molecular motions, especially in complex fluids. It thus appeared advisable to combine these two technologies to enable multifrequency 2D ELDOR studies of molecular motions. In fact, we are currently engaged in developing this methodology by implementing 2D ELDOR at 95 GHz. The technology available for 95 GHz 3 mm waves is not as well developed as that for microwaves in the 9-17 GHz regime. However, we demonstrated feasibility by developing a 95 GHz high-power pulse spectrometer based on quasioptical technology (Figs. 12 and 13).[19,20] This design utilizes a 1 kW extended interaction klystron (EIK) amplifier to generate intense and coherent nanosecond $\pi/2$ pulses, which are directed into a Fabry-Pérot resonator, into which the sample is placed. A block diagram of the spectrometer is shown in Fig. 14.

Previous studies of oriented samples,[20] which in general have a more limited spectral extent than non-oriented samples, have enabled us to demonstrate two distinct benefits. First, enhanced resolution is available from 2D ELDOR spectroscopy, and second, 95 GHz does yield an increased ability to discriminate between g- and hf- anisotropies, relative to 2D spectroscopy at lower frequencies. However, these early studies also highlighted two important challenges. First, we expect (as can be deduced from Fig. 10) a spectral extent of

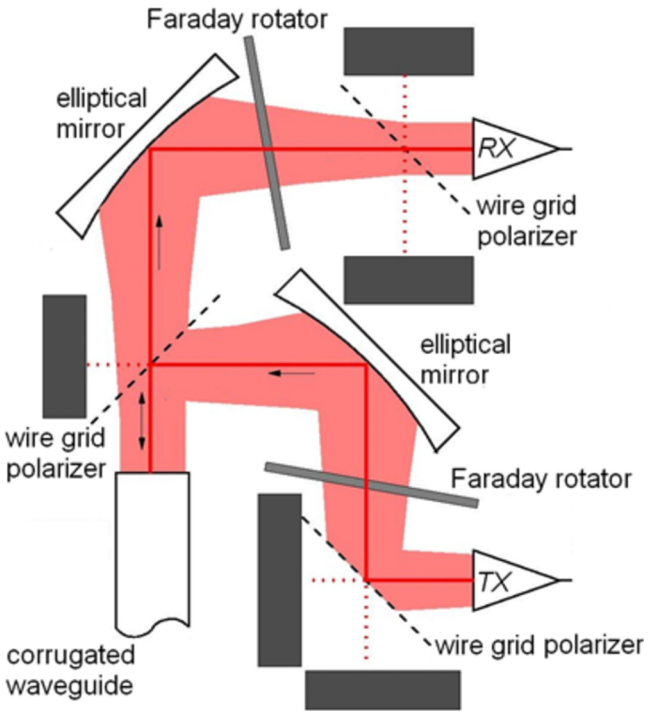

FIG. 12. Schematic diagram of a typical quasioptical bridge: A quasioptical beam is launched from the transmitter (Tx) at the bottom right of the figure, reflected off the wire-grid polarizer, and directed into the corrugated waveguide. The reflected signal that has orthogonal polarization to the transmitted pulse passes through the first wire-grid polarizer, where it is focused by the mirror onto the receiver (Rx). The second wire-grid polarizer and the associated Faraday rotator (at the top of the figure) provide additional isolation between the signal and the transmitted pulses. Adapted with permission from Fig. 8 of Earle *et al.*, Magn. Reson. Chem. **43**, S256 (2005). Copyright 2005 by John Wiley & Sons, Ltd.

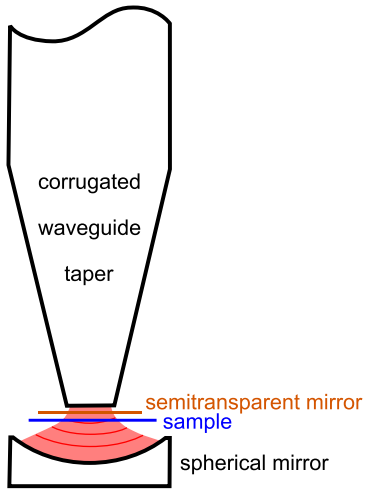

FIG. 13. The ESR probehead: differential screw drives attached to the various components allow simultaneous adjustment of the resonant frequency (via the mirror adjustment) characteristic impedance (via the semitransparent mirror/mesh adjustment) and sample positioning. Adapted with permission from Fig. 8 of K. A. Earle *et al.*, Magn. Reson. Chem. **43**, S256 (2005). Copyright 2005 by John Wiley & Sons, Ltd.

up to 135 G, or 380 MHz, making it a challenge to excite the full spectral bandwidth. Second, the much shorter T_2 decays at 95 GHz (Fig. 15) require a spectrometer to transition from a high power, pulsing mode to a low-power, signal detection mode in significantly less time. Our research thus focused on improvements in shortening the spectrometer dead times after the intense pulses and increasing the effective mm-wave pulsed magnetic field strength at the sample. The former is important in order to be able to observe the rapidly decaying signals, while the need for spectral coverage over the full range of spectral frequencies drives the latter.

Recently, various improvements have led to the reduction in dead time from ~50 ns to ~20–30 ns. The most significant of these involved reducing the jitter associated with the

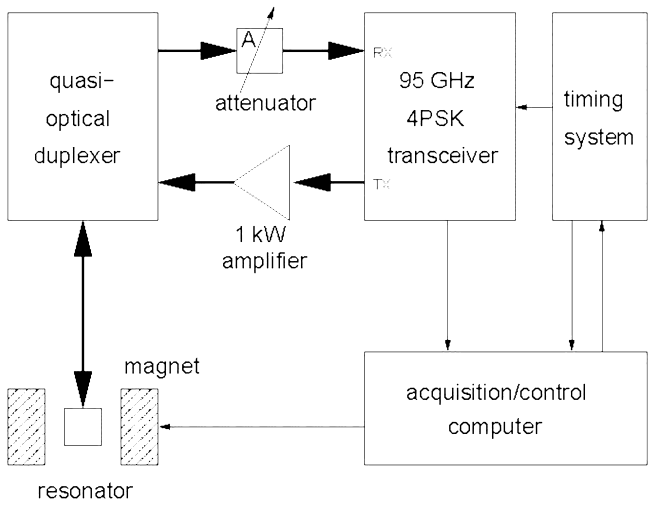

FIG. 14. Reprinted with permission from W. Hofbauer *et al.*, Rev. Sci. Instrum. **75**, 1194 (2004). Copyright 2004 by AIP Publishing LLC. Spectrometer block diagram. The low-power (90 mW) transmitter-receiver is augmented with a 1 kW mm-wave amplifier (EIK). Transmit and receive signal paths are duplexed in a quasioptical setup, as shown in Fig. 12.

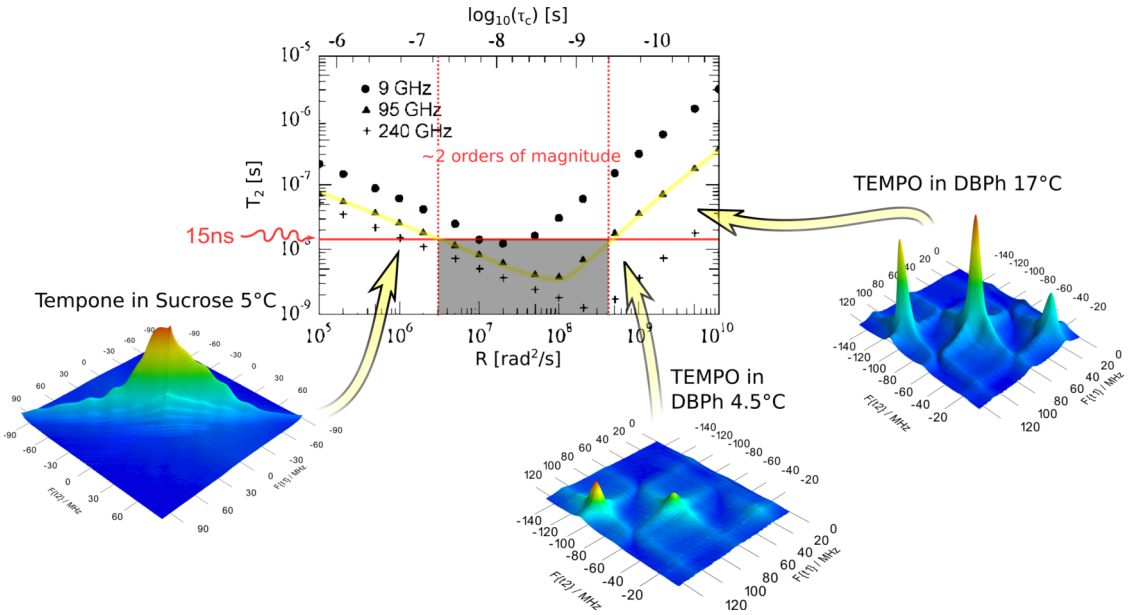

FIG. 15. For an isotropically tumbling nitroxide, the T_2 decay time will exhibit a minimum as the system transitions from the rigid limit (very slow tumbling) to the rapidly tumbling limit. As the ESR frequency increases, this minimum T_2 time shifts to faster tumbling rates and smaller absolute values. At 95 GHz, it is 10^8 s^{-1} and 4 ns, respectively. The rectangular box shows the range of motional rates—spanning approximately 2 orders of magnitude—that are inaccessible with the current dead times. The experimental spectra shown underneath are examples of data acquired outside this range. (Black inset simulation of T_2 *vs.* correlation time from Ref. 20; adapted with permission from Fig. 9 of K. A. Earle *et al.*, Magn. Reson. Chem. **43**, S256 (2005). Copyright 2005 by John Wiley & Sons, Ltd.)

high-voltage modulator that supplies power to the EIK amplifier. The resulting state-of-the-art detection system has allowed us to access signals with T_2 decay times as short as 15 ns, as illustrated in Fig. 16. However, this is still a significant limitation since, as shown in Fig. 15, for nitroxides, one expects T_2 times at 95 GHz to drop to values as low as 4 ns. One strategy around the present limitation involves choosing small, untethered spin probes that migrate to various portions of a chemical system. In a recent study, we dissolved small spin probes in a solution of lipid vesicles. The increased resolution of 95 GHz 2D ELDOR allowed us to easily discriminate two separate spectral components arising from the spin label dissolved in lipid *vs.* free solution (Fig. 17).

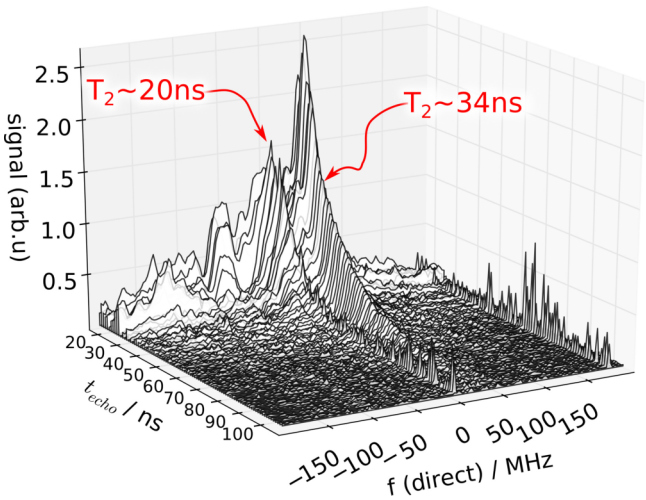

FIG. 16. A spin-echo experiment, acquired with 7 min of signal averaging from a sample of 1.5 mM TEMPO dissolved in dibutyl pthalate at 17 °C, measures the T_2 decay (along t_{echo}) of the signal amplitude across all frequency components, f, of the spectrum. Note how the spectral component with ~ 20 ns is close to the detection threshold. This component has approximately half the signal to noise of the ~34 ns component.

In a second, contrasting strategy, we can observe samples with relatively immobilized spin labels. Specifically, in the very slow motional regime (the left side of Fig. 15), useful experiments can be conducted. As previously discussed, 2D ELDOR permits us to separate the homogeneous and inhomogeneous broadening of the spectrum. Thus, one still expects a detailed characterization of the molecular dynamics near the spin probe, yielding the dynamical and ordering parameters previously mentioned. In addition, one can probe longer time scale molecular motions by observing the development of the inhomogeneities on the time scale of tens of microseconds (i.e., limited only by T_1 relaxation during T_m).[23,59] As in the previous cw-ESR multi-frequency experiments, a multi-frequency analysis (e.g., also at 17 GHz and 95 GHz) will offer improved resolution of structure and dynamics on several time scales.

As a crucial step towards implementing this strategy, we have begun to optimize the mm-wave B_1 field strength at the sample, in order to achieve excitation coverage over a significant portion of the inhomogeneously broadened spectrum. While previously a B_1 field strength of 18 G was achieved, this has now been increased to ≥28 G, a gain that comes principally by developing an optimized sample holder constructed from sapphire, which has a higher index of refraction than the previously employed quartz. Initial simulations with the 3D electromagnetic field simulator HFSS (high field structure simulator, Ansys, Canonsburg, PA) identified three key design criteria for the disk-shaped sample holder: (1) the diameter of the disk must significantly exceed the diameter of the quasioptical mm-wave beam, (2) the

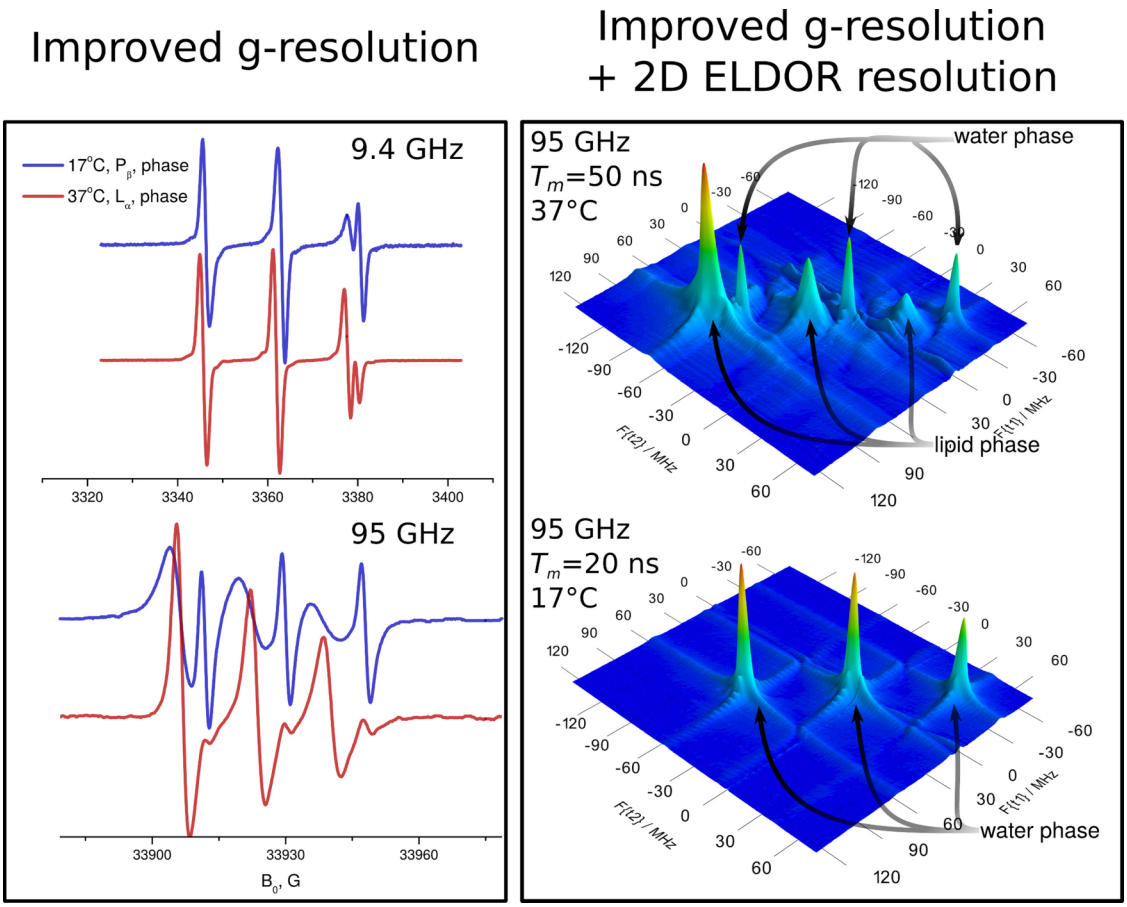

FIG. 17. Signal from a sample of 1 mM TEMPO partitioned between water and 1,2-dimyristoyl-*sn*-glycero-3-phosphocholine (DMPC). In contrast to a typical 9.4 GHz cw spectrum (top left panel), the spectrum at 95 GHz (bottom left pane) demonstrates the benefits of the increased g-anisotropy, permitting a better distinction between nitroxides in the lipid *vs* water phase, leading to noticeable changes in the spectra at different temperatures. The extra dimension of 2D ELDOR allows separation of the peaks arising from the nitroxide partitioning in the two different phases. Note that at 17 °C, we begin to see the limitations of the current state-of-the-art—the signal with shorter T_2 from the TEMPO in the lipid phase decays during the spectrometer dead time before detection of the 2D ELDOR signal begins, leaving only signal from the component that resides in the water.

thickness of the disk must be chosen to minimize reflections at the surface of the sample holder, and (3) the sample should be placed at the center of the disk, where the B_1 field is maximal. We then optimized criterion (2) by employing the transfer matrix method (TMM), by which the boundary-matching problem for the E field of a plane wave and its derivative is solved, in order to determine the reflection and transmission through our sample holder. We find that the optimal sample holder consists of a disk of sapphire with a half-wavelength thickness: $0.5c/(95 \times 10^9\ \text{Hz}\sqrt{\varepsilon_{r,sapphire}}) \approx 500\ \mu$m. In order to insert the sample into this disk, we must split the disk and create a central void where the sample is inserted; TMM calculations tell us that the reflections at the surface of the sample holder are critically dependent on the relative size of this void and the sapphire slices. Thus, we should be able to and are currently working to further optimize the sample holder and achieve even higher B_1 amplitudes. In combination with advances to our temperature control system that permit us to perform 2D ELDOR at temperatures as low as −100 °C, the increased coverage will be valuable for studying a wide range of very slow-motional dynamics and structure.

We have found that the increased spectral resolution obtained by 2D ELDOR at 95 GHz comes with a price as far as their simulation is concerned, especially for the 2D spectra at slower motions. Our standard method for computation of the SLE described above, utilizing the LA, breaks down in this regime, because of serious convergence issues due to computer round-off errors. This is a greater problem for 95 GHz spectra than for lower frequencies. However, we have made significant progress towards enabling the simulation of high-frequency 2D ELDOR over the whole motional range. In particular, an improved LA based on the quasi-minimum residuals (LA-QMR) method replaces the LA-CG (conjugate gradients) method we have previously been using.[50]

VI. CONCLUSION

A multifrequency analysis has proven very successful with cw ESR spectroscopy, where frequencies of 95 GHz and above report on molecular motion in the slow-motional regime. The current state-of-the-art is on the verge of overcoming technological challenges that will allow one to perform a 2D ELDOR variant of the multifrequency approach. Multifrequency 2D ELDOR is now effectively a four-dimensional method, as it includes two additional, useful dimensions: (1) the 2D ELDOR storage period T_m that allows one to track motions over the tens of microsecond time scale and (2) variation of the resonance frequency that allows one to

sensitively probe molecular motion on different time scales. The capability to separate global and local motions has been demonstrated, as has the ability to resolve localized changes in phase behavior in complex systems, and to perform a highly detailed characterization of molecular motion and ordering in aligned samples. With further key improvements to 2D ELDOR at 95 GHz, enhanced capabilities should follow.

ACKNOWLEDGMENTS

This work is supported by Grant No. P41GM103521 (NIGMS/NIH) from the National Institute of General Medical Sciences (NIGMS). Ongoing projects related to electron spin relaxation in membranes are supported by Grant No. R01EB003150 from the National Institute of Biomedical Imaging and Bioengineering (NIBIB/NIH). We would like to thank Professor P. Petersen for useful discussions regarding comparisons to other forms of spectroscopy. Research on improved B_1 fields was performed as part of a collaboration with S. Y. El Naggar and S. M. Mattar at the University of New Brunswick and K. A. Earle, SUNY Albany.

[1]P. P. Borbat, A. J. Costa-Filho, K. A. Earle, J. K. Moscicki, and J. H. Freed, Science **291**, 266 (2001).
[2]P. Borbat and J. Freed, in *Structural Information from Spin-Labels and Intrinsic Paramagnetic Centres in the Biosciences*, Structure and Bonding Vol. 152, edited by C. R. Timmel and J. R. Harmer (Springer, Berlin, Heidelberg, 2013), pp. 1–82.
[3]W. L. Hubbell, C. J. López, C. Altenbach, and Z. Yang, Curr. Opin. Struct. Biol. **23**, 725 (2013).
[4]A. Polimeno, V. Barone, and J. H. Freed, in *Computational Spectroscopy*, edited by V. Barone (Wiley, NY, 2012), Chap. 12, pp. 549–582.
[5]J. H. Freed, in *Biomedical EPR, Part B: Methodology, Instrumentation, and Dynamics*, Biological Magnetic Resonance Vol. 24/B, edited by S. Eaton, G. Eaton, and L. Berliner (Springer, New York, 2005), pp. 239–268.
[6]S. K. Misra and J. H. Freed, "Molecular motions," in *Multifrequency Electron Paramagnetic Resonance* (Wiley-VCH Verlag GmbH & Co. KGaA, 2011), pp. 497–544.
[7]G. Jeschke, Prog. Nucl. Magn. Reson. Spectrosc. **72**, 42 (2013).
[8]W. B. Lynch, K. A. Earle, and J. H. Freed, Rev. Sci. Instrum. **59**, 1345 (1988).
[9]K. A. Earle, J. K. Moscicki, A. Polimeno, and J. H. Freed, J. Chem. Phys. **106**, 9996 (1997).
[10]J. H. Freed, in *Very High Frequency (VHF) ESR/EPR*, Biological Magnetic Resonance Vol. 22, edited by O. Y. Grinberg and L. J. Berliner (Springer, US, 2004), pp. 19–43.
[11]D. Sezer, J. H. Freed, and B. Roux, J. Am. Chem. Soc. **131**, 2597 (2009).
[12]Z. Zhang, M. R. Fleissner, D. S. Tipikin, Z. Liang, J. K. Moscicki, K. A. Earle, W. L. Hubbell, and J. H. Freed, J. Phys. Chem. B **114**, 5503 (2010).
[13]J. H. Freed, Annu. Rev. Phys. Chem. **51**, 655 (2000).
[14]S. Lee, B. R. Patyal, S. Saxena, R. H. Crepeau, and J. H. Freed, Chem. Phys. Lett. **221**, 397 (1994).
[15]D. J. Xu, R. H. Crepeau, C. K. Ober, and J. H. Freed, J. Phys. Chem. **100**, 15873 (1996).
[16]V. S. S. Sastry, A. Polimeno, R. H. Crepeau, and J. H. Freed, J. Chem. Phys. **105**, 5753 (1996).
[17]A. J. Costa-Filho, Y. Shimoyama, and J. H. Freed, Biophys. J. **84**, 2619 (2003).
[18]Y.-W. Chiang, A. J. Costa-Filho, J. H. Freed, Y. W. Chiangs, A. J. Costa-Filho, and J. H. Freed, J. Phys. Chem. B **111**, 11260 (2007).
[19]W. Hofbauer, K. A. Earle, C. R. Dunnam, J. K. Moscicki, and J. H. Freed, Rev. Sci. Instrum. **75**, 1194 (2004).
[20]K. A. Earle, B. Dzikovski, W. Hofbauer, J. K. Moscicki, and J. H. Freed, Magn. Reson. Chem. **43**, S256 (2005).
[21]P. A. S. Cruickshank, D. R. Bolton, D. A. Robertson, R. I. Hunter, R. J. Wylde, and G. M. Smith, Rev. Sci. Instrum. **80**, 103102 (2009).
[22]D. J. H. Schneider and J. H. Freed, Adv. Chem. Phys. **LXXIII**, 387 (1989).
[23]S. Lee, D. E. Budil, and J. H. Freed, J. Chem. Phys. **101**, 5529 (1994).
[24]R. M. Hochstrasser, Nature **434**, 570 (2005).
[25]D. Zhong, S. K. Pal, and A. H. Zewail, Chem. Phys. Lett. **503**, 1 (2011).
[26]M. D. Fayer and N. E. Levinger, Annu. Rev. Anal. Chem. (Palo Alto, Calif.) **3**, 89 (2010).
[27]K. Ramasesha, L. De Marco, A. Mandal, and A. Tokmakoff, Nat. Chem. **5**, 935 (2013).
[28]G. Pabst, A. Hodzic, J. Strancar, S. Danner, M. Rappolt, and P. Laggner, Biophys. J. **93**, 2688 (2007).
[29]E. Meirovitch, A. Nayeem, and J. H. Freed, J. Phys. Chem. **88**, 3454 (1984).
[30]H. J. Steinhoff, R. Mollaaghababa, C. Altenbach, K. Hideg, M. Krebs, H. G. Khorana, and W. L. Hubbell, Science **266**, 105 (1994).
[31]M. Ge and J. H. Freed, Biophys. J. **65**, 2106 (1993).
[32]V. S. S. Sastry, A. Polimeno, R. H. Crepeau, and J. H. Freed, J. Chem. Phys. **105**, 5773 (1996).
[33]W. P. Aue, E. Bartholdi, and R. R. Ernst, J. Chem. Phys. **64**, 2229 (1976).
[34]J. Jeener, B. H. Meier, P. Bachmann, and R. R. Ernst, J. Chem. Phys. **71**, 4546 (1979).
[35]J. Hyde, J. Chien, and J. Freed, J. Chem. Phys. **48**, 4211 (1968).
[36]J. Gorcester and J. H. Freed, J. Chem. Phys. **85**, 5375 (1986).
[37]U. Eliav and J. H. Freed, J. Phys. Chem. **88**, 1277 (1984); Y. Panferov, O. Grinberg, A. Dubinskii, and Y. Lebedev, Dokl. Phys. Chem. **278**, 888–890 (1984); O. Dobbert, T. Prisner, and K. Dinse, J. Magn. Reson. **70**, 173–175 (1986).
[38]A. Angerhofer, R. J. Massoth, and M. K. Bowman, Isr. J. Chem. **28**, 227 (1988).
[39]J. Gorcester and J. H. Freed, J. Chem. Phys. **88**, 4678 (1988).
[40]J. Gorcester, B. Rananavare, and J. H. Freed, J. Chem. Phys. **90**, 5764 (1989).
[41]B. R. Patyal, R. H. Crepeau, D. Gamliel, and J. H. Freed, Chem. Phys. Lett. **175**, 445 (1990).
[42]B. R. Patyal, R. H. Crepeau, D. Gamliel, and J. H. Freed, Chem. Phys. Lett. **175**, 453 (1990).
[43]R. H. Crepeau, S. Saxena, S. Lee, B. Patyal, and J. H. Freed, Biophys. J. **66**, 1489 (1994).
[44]J. H. Freed, G. V. Bruno, and C. F. Polnaszek, J. Phys. Chem. **75**, 3385 (1971).
[45]G. J. Moro and J. H. Freed, J. Chem. Phys. **74**, 3757 (1981); L. J. Schwartz, A. E. Stillman, and J. H. Freed, *ibid.* **77**, 5410 (1982); Z. Liang, R. H. Crepeau, and J. H. Freed, J. Magn. Reson. **177**, 247 (2005).
[46]D. J. Schneider and J. H. Freed, in *Spin Labeling—Theory and Applications*, Biological Magnetic Resonance Vol. 8, edited by L. J. Berliner and J. Reuben (Plenum Press, New York, 1989), pp. 1–76.
[47]E. Meirovitch, D. Igner, E. Igner, G. Moro, and J. H. Freed, J. Chem. Phys. **77**, 3915 (1982).
[48]A. Polimeno and J. H. Freed, J. Phys. Chem. **99**, 10995 (1995).
[49]Z. Liang and J. H. Freed, J. Phys. Chem. B **103**, 6384 (1999).
[50]Y. W. Chiang and J. H. Freed, J. Chem. Phys. **134**, 034112 (2011).
[51]A. Polimeno and J. H. Freed, Adv. Chem. Phys. **83**, 89 (1993).
[52]A. J. Costa-Filho, R. H. Crepeau, P. P. Borbat, M. Ge, and J. H. Freed, Biophys. J. **84**, 3364 (2003).
[53]P. P. Borbat, R. H. Crepeau, and J. H. Freed, J. Magn. Reson. **127**, 155 (1997).
[54]Y.-W. Chiang, A. Costa-Filho, and J. H. Freed, J. Magn. Reson. **188**, 231 (2007).
[55]S. Saxena and J. H. Freed, J. Magn. Reson. **124**, 439 (1997).
[56]Y. W. Chiang, A. J. Costa-Filho, and J. H. Freed, Appl. Magn. Reson. **31**, 375 (2007).
[57]Y.-W. Chiang, A. J. Costa-Filho, B. Baird, and J. H. Freed, J. Phys. Chem. B **115**, 10462 (2011).
[58]D. E. Budil, K. A. Earle, and J. H. Freed, J. Phys. Chem. **97**, 1294 (1993).
[59]S. Saxena and J. H. Freed, J. Phys. Chem. A **101**, 7998 (1997).